

Fractures and induced anisotropy in poroelastic media. From the Mesoscale to the Macroscale

Juan E. Santos

Instituto del Gas y del Petróleo, **Facultad de Ingeniería UBA, CONICET** and Department of Mathematics, **Purdue University** and Universidad Nacional de La Plata (**UNLP**)

Work in collaboration with J.M. Carcione (**OGS**), P. M. Gauzellino (**UNLP**) and R. Martínez Corredor (**UNLP**)

**IV International Conference on Approximation Methods for Design and Control,
November 5th 2015**

- A planar fracture embedded in a fluid-saturated poroelastic – Biot - medium can be modeled as a extremely thin, highly permeable and compliant porous layer.
- A Biot medium containing a dense set of aligned fractures behaves as an effective transversely isotropic and viscoelastic (TIV) medium when the average fracture distance is much smaller than the predominant wavelength of the traveling waves.
- This leads to frequency and angular variations of velocity and attenuation of seismic waves.

- P-waves traveling in this type of medium induce fluid-pressure gradients at fractures and mesoscopic-scale heterogeneities, generating fluid flow and slow (diffusion) Biot waves, causing attenuation and dispersion of the fast modes (mesoscopic loss).
- A poroelastic medium with embedded aligned fractures exhibits significant attenuation and dispersion effects due to this mechanism.
- Due to the **extremely fine meshes** needed to properly represent these mesoscopic-scale fractures, numerical simulations are very expensive or even not feasible.

- **Our approach:** In the context of **Numerical Rock Physics**, we use a **numerical upscaling procedure** to determine the complex and frequency dependent stiffness at the macroscale of a TIV medium equivalent to a Biot medium with aligned fractures.
- To determine the **complex stiffness** coefficients of the **equivalent TIV medium at the macroscale**, we solve a set of boundary value problems (BVP's) for Biot's equation in the diffusive range.
- The BVP's are stated and solved in the space-frequency-domain using the finite-element method (**FEM**).

- The BVP's represent **harmonic tests** at a finite number of frequencies on a representative sample of the material.
- **Numerical Rock Physics** offer an alternative to laboratory measurements.
- Numerical experiments are inexpensive and informative since the physical process of wave propagation can be inspected during the experiment.
- Moreover, they are **repeatable, essentially free from experimental errors**, and may easily be run using alternative models of the rock and fluid properties.

The Mesoscale. Anisotropic poroelasticity. I

- For Biot's media, White et al. (1975) were the first to introduce the mesoscopic-loss mechanism in the framework of Biot's theory.
- For fine layered poroelastic materials, the theories of Gelinsky and Shapiro (GPY, 62, 1997) and Krzikalla and Müller (GPY, 76, 2011) allow to obtain the **five** complex and frequency-dependent stiffnesses of the **equivalent TIV medium**.
- To provide a more general modeling tool, we present a **numerical upscaling procedure** to obtain the complex stiffnesses of the effective **TIV** medium.

The Mesoscale. Anisotropic poroelasticity. II

- We employ the FEM to solve in the space-frequency domain **Biot's equations in the diffusive range** with boundary conditions representing **compressibility and shear harmonic** experiments.
- The methodology is applied to saturated isotropic poroelastic samples having a dense set of horizontal fractures.
- The samples contained mesoscopic-scale heterogeneities due to patchy brine-CO₂ saturation and fractal porosity and consequently, fractal permeability and frame properties.
- Applying a Bond transformation matrix, the macroscale stiffness coefficients can be used to represent fractures at any orientation.

The Mesoscale. Anisotropic poroelasticity. III

Let us consider isotropic fluid-saturated poroelastic layers.

$\mathbf{u}^s(\mathbf{x}), \mathbf{u}^f(\mathbf{x})$: time Fourier transform of the displacement vector of the solid and fluid relative to the solid frame, respectively.

$$\mathbf{u} = (\mathbf{u}^s, \mathbf{u}^f)$$

$\sigma_{kl}(u), \mathbf{p}_f(u)$: Fourier transform of the total stress and the fluid pressure, respectively

On each plane layer n in a sequence of N layers, the **frequency-domain stress-strain relations** are

$$\begin{aligned}\sigma_{kl}(u) &= 2\mu \varepsilon_{kl}(u^s) + \delta_{kl} (\lambda_G \nabla \cdot u^s + \alpha M \nabla \cdot u^f), \\ \mathbf{p}_f(u) &= -\alpha M \nabla \cdot u^s - M \nabla \cdot u^f.\end{aligned}$$

Biot's equations in the diffusive range:

$$\nabla \cdot \sigma(u) = 0,$$

$$i\omega \frac{\eta}{\kappa} u^f(x, \omega) + \nabla p_f(u) = 0,$$

$\omega = 2\pi f$: angular frequency

η : fluid viscosity

κ : frame permeability

The TIV medium at the Macroscale.

τ_{ij} : stress tensor of the equivalent TIV medium

For a **closed system** ($\nabla \cdot u^f = 0$), the corresponding **stress-strain relations**, stated in the space-frequency domain, are

$$\tau_{11}(u) = p_{11} \epsilon_{11}(u^s) + p_{12} \epsilon_{22}(u^s) + p_{13} \epsilon_{33}(u^s),$$

$$\tau_{22}(u) = p_{12} \epsilon_{11}(u^s) + p_{11} \epsilon_{22}(u^s) + p_{13} \epsilon_{33}(u^s),$$

$$\tau_{33}(u) = p_{13} \epsilon_{11}(u^s) + p_{13} \epsilon_{22}(u^s) + p_{33} \epsilon_{33}(u^s),$$

$$\tau_{23}(u) = 2 p_{55} \epsilon_{23}(u^s),$$

$$\tau_{13}(u) = 2 p_{55} \epsilon_{13}(u^s),$$

$$\tau_{12}(u) = 2 p_{66} \epsilon_{12}(u^s).$$

This approach provides the complex velocities of the fast modes and takes into account **interlayer flow effects**.

The harmonic experiments to determine the stiffness coefficients. I

To determine the complex stiffness we solve Biot's equation in the 2D case on a reference square $\Omega = (0, L)^2$ with boundary Γ in the (x_1, x_3) -plane. Set $\Gamma = \Gamma^L \cup \Gamma^B \cup \Gamma^R \cup \Gamma^T$, where

$$\Gamma^L = \{(x_1, x_3) \in \Gamma : x_1 = 0\}, \quad \Gamma^R = \{(x_1, x_3) \in \Gamma : x_1 = L\},$$

$$\Gamma^B = \{(x_1, x_3) \in \Gamma : x_3 = 0\}, \quad \Gamma^T = \{(x_1, x_3) \in \Gamma : x_3 = L\}.$$

The harmonic experiments to determine the stiffness coefficients. II

The sample is subjected to **harmonic compressibility and shear tests** described by the following sets of **boundary conditions**.

$\mathcal{P}_{33}(\omega)$:

$$\sigma(u)\nu \cdot \nu = -\Delta P, \quad (x_1, x_3) \in \Gamma^T,$$

$$\sigma(u)\nu \cdot \chi = 0, \quad (x_1, x_3) \in \Gamma,$$

$$u^s \cdot \nu = 0, \quad (x_1, x_3) \in \Gamma \setminus \Gamma^T,$$

$$u^f \cdot \nu = 0, \quad (x_1, x_3) \in \Gamma.$$

ν : the unit outer normal on Γ

χ : a unit tangent on Γ so that $\{\nu, \chi\}$ is an orthonormal system on Γ .

Denote by V the original volume of the sample and by $\Delta V(\omega)$ its (complex) oscillatory volume change.

The harmonic experiments to determine the stiffness coefficients. III

In the quasistatic case

$$\frac{\Delta V(\omega)}{V} = -\frac{\Delta P}{p_{33}(\omega)},$$

Then after computing the average $u_3^{s,T}(\omega)$ of the vertical displacements on Γ^T , we approximate

$$\Delta V(\omega) \approx Lu_3^{s,T}(\omega)$$

which enable us to compute $p_{33}(\omega)$

To determine $p_{11}(\omega)$ we solve an identical boundary value problem than for p_{33} but for a 90° rotated sample.

The harmonic experiments to determine the stiffness coefficients. IV

$p_{55}(\omega)$: the boundary conditions are

$$-\sigma(u)\nu = g, \quad (x_1, x_3) \in \Gamma^T \cup \Gamma^L \cup \Gamma^R,$$

$$u^s = 0, \quad (x_1, x_3) \in \Gamma^B,$$

$$u^f \cdot \nu = 0, \quad (x_1, x_3) \in \Gamma,$$

where

$$g = \begin{cases} (0, \Delta G), & (x_1, x_3) \in \Gamma^L, \\ (0, -\Delta G), & (x_1, x_3) \in \Gamma^R, \\ (-\Delta G, 0), & (x_1, x_3) \in \Gamma^T. \end{cases}$$

The harmonic experiments to determine the stiffness coefficients. V

The change in shape suffered by the sample is

$$\tan[\theta(\omega)] = \frac{\Delta G}{p_{55}(\omega)}. \quad (1)$$

$\theta(\omega)$: the angle between the original positions of the lateral boundaries and the location after applying the shear stresses.

Since

$\tan[\theta(\omega)] \approx u_1^{s,T}(\omega)/L$, where $u_1^{s,T}(\omega)$ is the average horizontal displacement at Γ^T , $p_{55}(\omega)$ can be determined from

to determine $p_{66}(\omega)$ (shear waves traveling in the (x_1, x_2) -plane), we rotate the layered sample 90° and apply the shear test as indicated for $p_{55}(\omega)$.

The harmonic experiments to determine the stiffness coefficients. VI

$p_{13}(\omega)$: the boundary conditions are

$$\sigma(u)\nu \cdot \nu = -\Delta P, \quad (x_1, x_3) \in \Gamma^R \cup \Gamma^T,$$

$$\sigma(u)\nu \cdot \chi = 0, \quad (x_1, x_3) \in \Gamma,$$

$$u^s \cdot \nu = 0, \quad (x_1, x_3) \in \Gamma^L \cup \Gamma^B, \quad u^f \cdot \nu = 0, \quad (x_1, x_3) \in \Gamma.$$

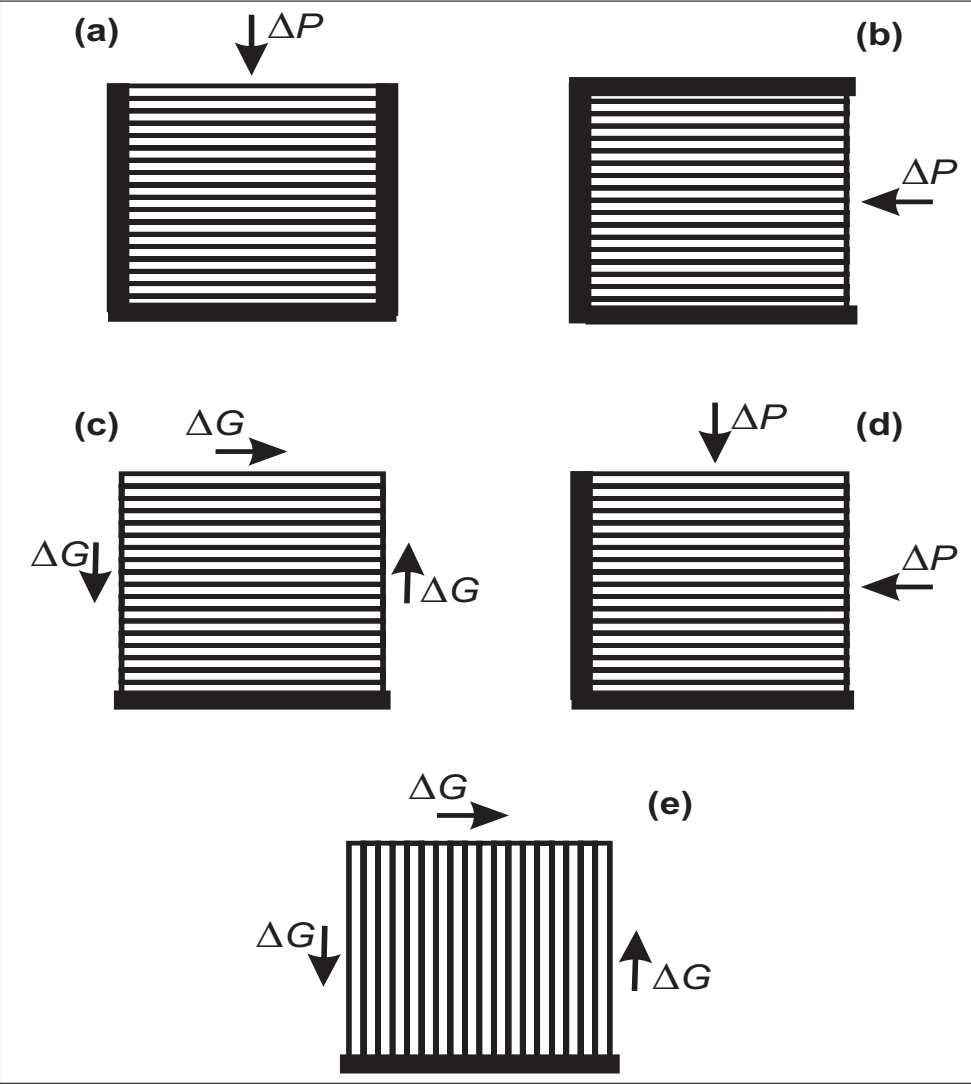
In this experiment $\epsilon_{22} = \nabla \cdot u^f = 0$, so that

$$\tau_{11} = p_{11}\epsilon_{11} + p_{13}\epsilon_{33}, \quad \tau_{33} = p_{13}\epsilon_{11} + p_{33}\epsilon_{33}, \quad (2)$$

$\epsilon_{11}, \epsilon_{33}$: the strain components at the right lateral side and top side of the sample, respectively. Then,

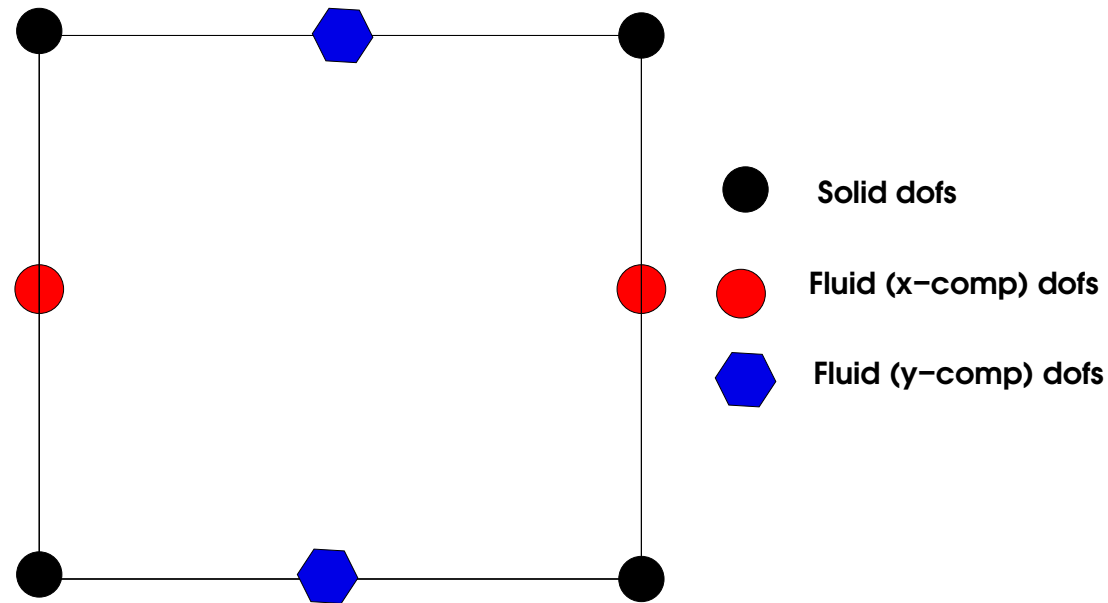
$$p_{13}(\omega) = (p_{11}\epsilon_{11} - p_{33}\epsilon_{33}) / (\epsilon_{11} - \epsilon_{33}).$$

Schematic representation of the oscillatory compressibility and shear tests.



a): p_{33} , b): p_{11} , c): p_{55} , d): p_{13} e): p_{66}

Local degrees of freedom for the FEM solution of the harmonic tests.



The solution of the oscillatory tests was computed using the **FEM**. The figure displays the local degrees of freedom (**DOFs**) associated with each component of the solid displacement and the fluid displacement vectors. Once we computed the p_{IJ} coefficients, we can determine the velocities and attenuation factors of the equivalent TIV medium.

Complex velocities of the equivalent TIV anisotropic medium:

$$v_{qP} = (2\bar{\rho})^{-1/2} \sqrt{p_{11}l_1^2 + p_{33}l_3^2 + p_{55} + A},$$

$$v_{qSV} = (2\bar{\rho})^{-1/2} \sqrt{p_{11}l_1^2 + p_{33}l_3^2 + p_{55} - A},$$

$$v_{SH} = \bar{\rho}^{-1/2} \sqrt{p_{66}l_1^2 + p_{55}l_3^2},$$

$$A = \sqrt{[(p_{11} - p_{55})l_1^2 + (p_{55} - p_{33})l_3^2]^2 + 4[(p_{13} + p_{55})l_1l_3]^2}.$$

$\bar{\rho} = \langle \rho \rangle$: **average bulk density,**

$l_1 = \sin \theta$, $l_3 = \cos \theta$ **are the directions cosines, θ is the propagation angle between the wavenumber vector and the x_3 -symmetry axis and the three velocities correspond to the qP, qS and SH waves, respectively.**

The seismic phase velocity and quality factors are:

$$v_p = \left[\operatorname{Re} \left(\frac{1}{v} \right) \right]^{-1} \quad \text{and} \quad Q = \frac{\operatorname{Re}(v^2)}{\operatorname{Im}(v^2)},$$

where v represents either v_{qP} , v_{qSV} or v_{SH} .

The energy-velocity vector \mathbf{v}_e of the qP and qSV waves is

$$\frac{\mathbf{v}_e}{v_p} = (l_1 + l_3 \cot \psi)^{-1} \hat{\mathbf{e}}_1 + (l_1 \tan \psi + l_3)^{-1} \hat{\mathbf{e}}_3,$$

ψ : angle between the energy-velocity vector and the x_3 -axis.

The energy velocity of the SH wave is

$$\mathbf{v}_e = \frac{1}{\bar{\rho} v_p} (l_1 p_{66} \hat{\mathbf{e}}_1 + l_3 p_{55} \hat{\mathbf{e}}_3).$$

The Mesoscale. Examples. I

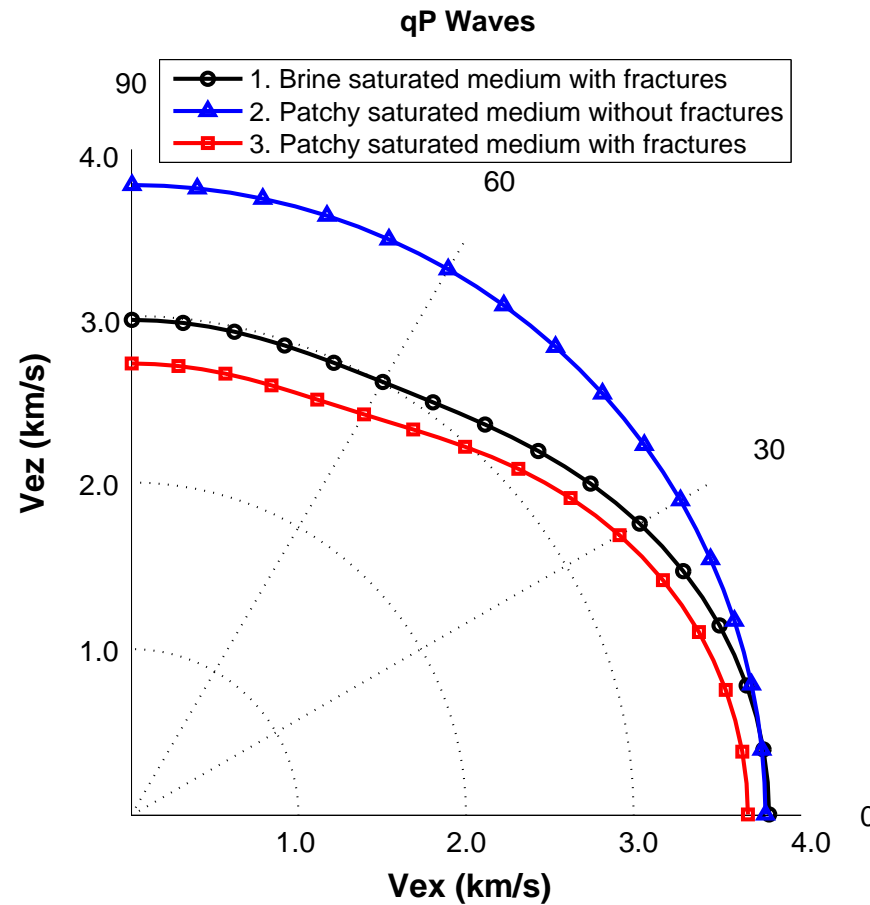
A set of numerical examples consider the following cases for a square poroelastic sample of 160 cm side length and 10 periods of 1 cm fracture, 15 cm background:

- Case 1: A brine-saturated sample with fractures.
- Case 2: A brine-CO₂ patchy saturated sample without fractures.
- Case 3: A brine-CO₂ patchy saturated sample with fractures.
- Case 4: A brine saturated sample with a fractal frame and fractures.

The discrete boundary value problems to determine the complex stiffnesses $p_{IJ}(\omega)$ were solved for 30 frequencies using a public domain sparse matrix solver package.

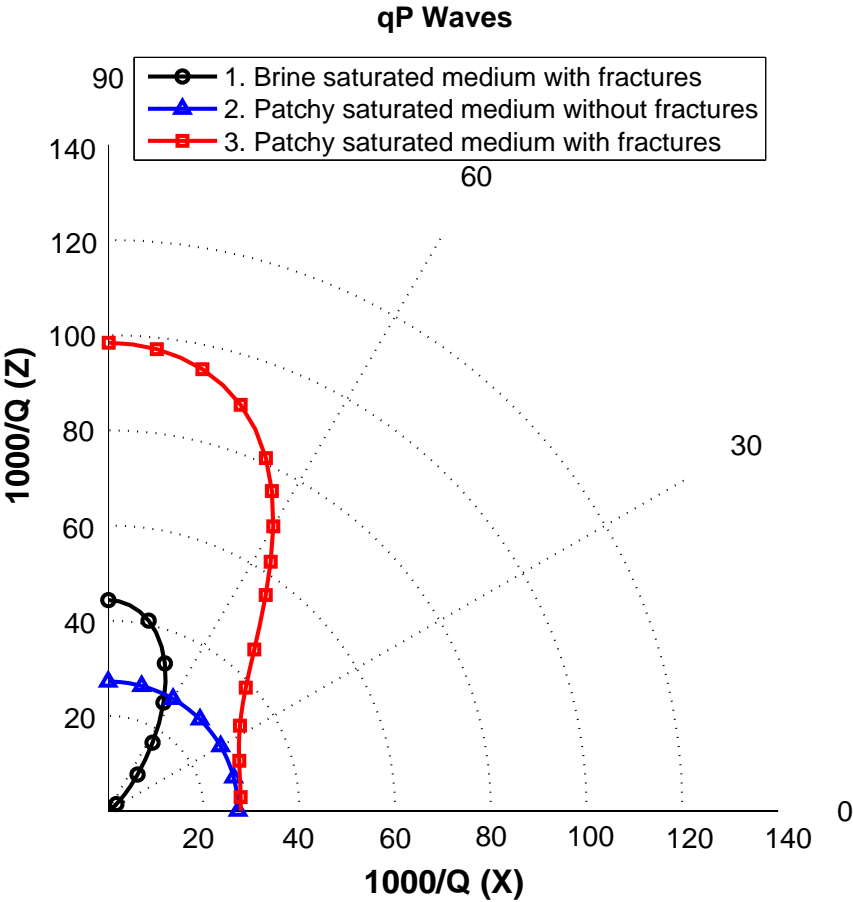
The $p_{IJ}(\omega)$'s determine in turn the energy velocities and dissipation coefficients shown in the next figures.

Polar representation of the qP energy velocity vector at 50 Hz for cases 1, 2 and 3



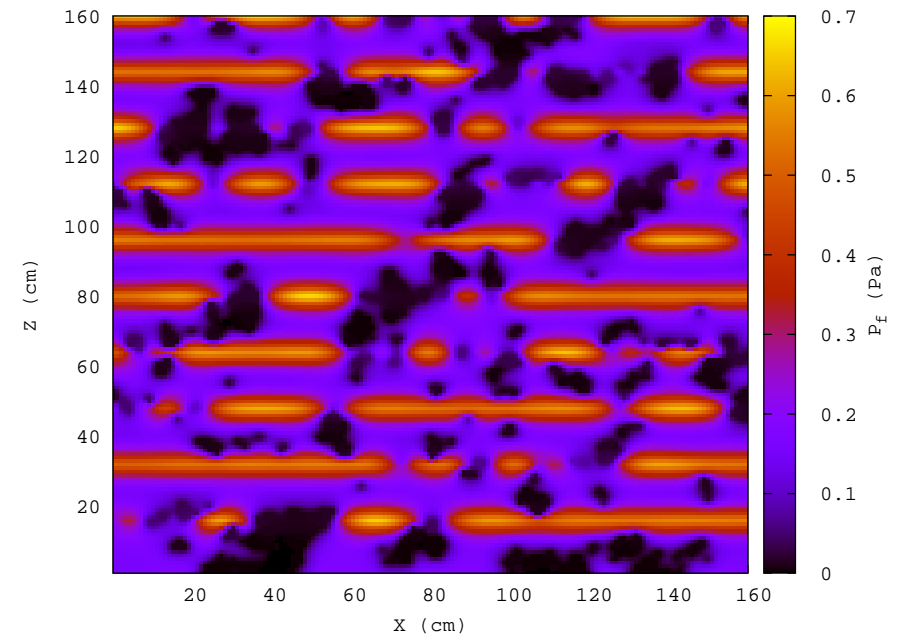
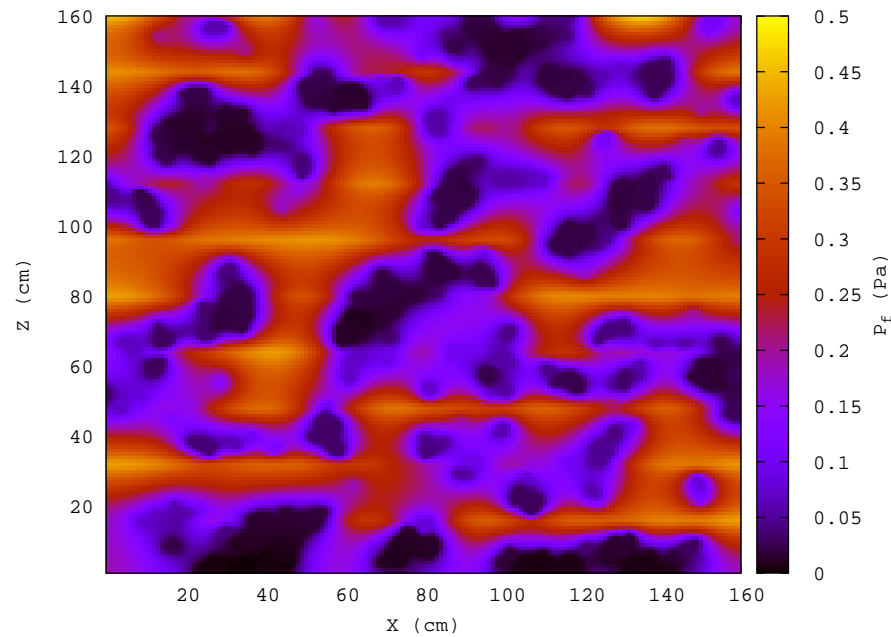
Velocity anisotropy caused by the fractures in cases 1 and 3 is enhanced for the case of patchy saturation, with lower velocities when patches are present. The velocity behaves isotropically in case 2.

Dissipation factor of the qP waves at 50 Hz for cases 1, 2 and 3



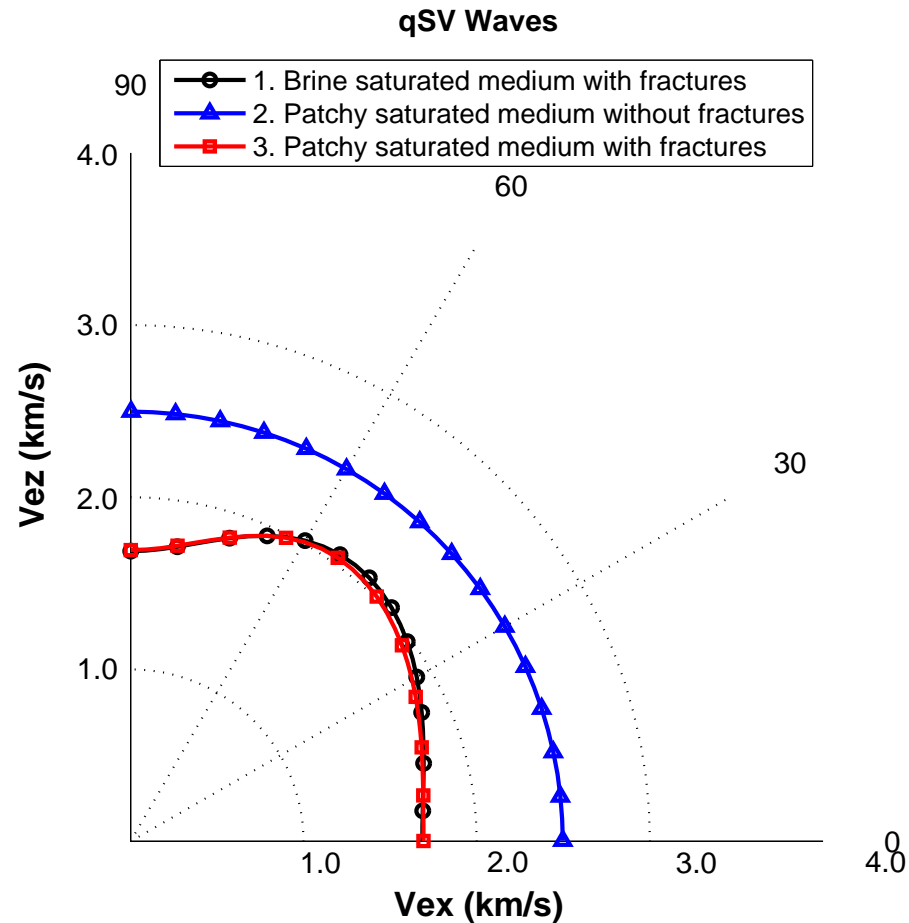
Fractures induce strong Q anisotropy for angles normal to the fracture plane, enhanced by patchy saturation.

Fluid pressure distribution at 50 and 300 Hz. Compressibility test for p_{33} for case 3.



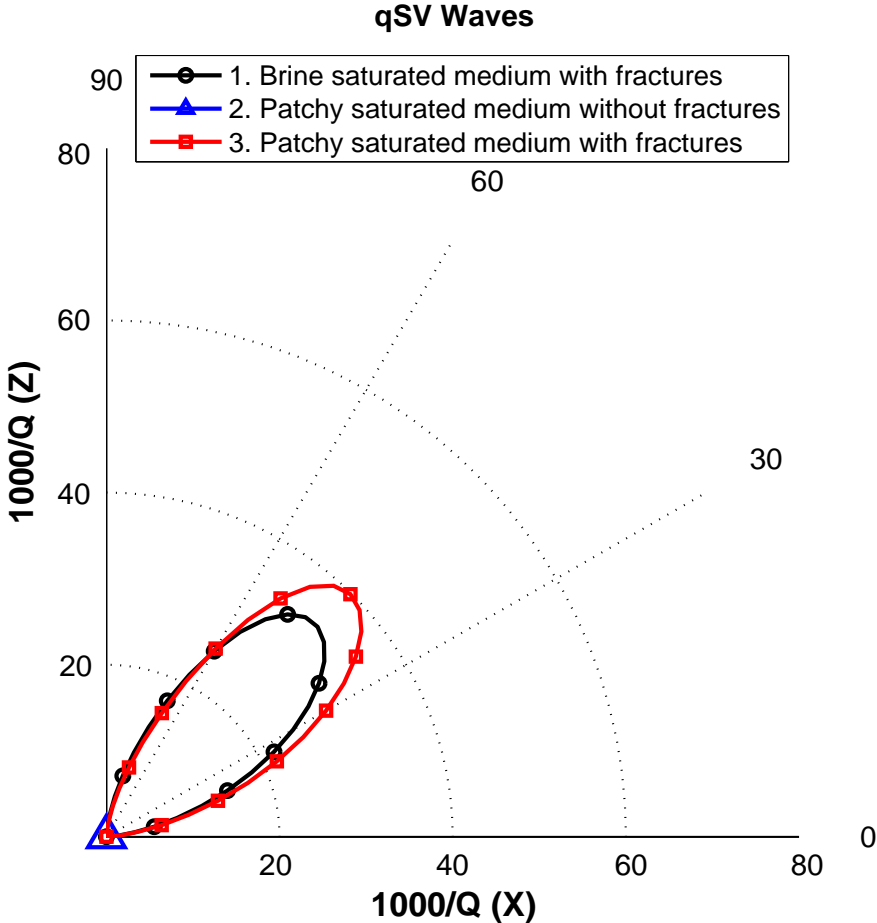
Compression is normal to the fracture plane. Attenuation is stronger at 300 Hz.

Polar representation of the qSV energy velocity vector at 50 Hz for cases 1, 2 and 3



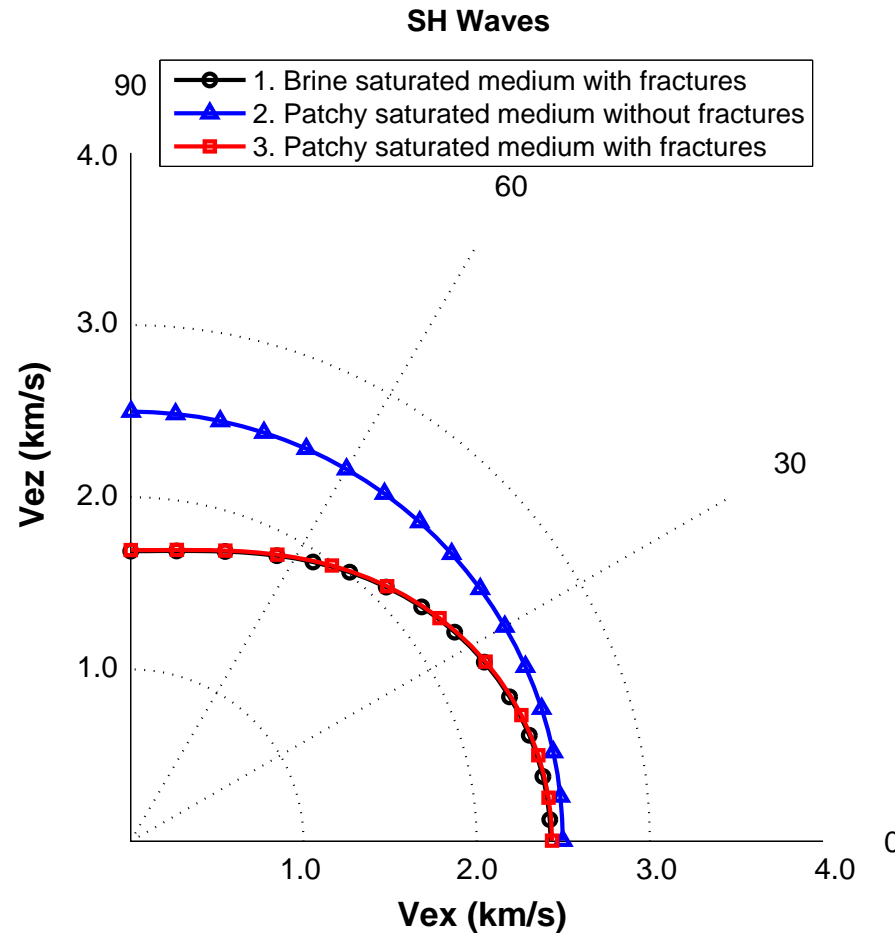
Velocity anisotropy is induced by fractures (cases 1 and 3). Patchy saturation does not affect the anisotropic behavior of the qSV velocities. Case 2 shows isotropic velocity, with higher velocity values than for the fractured cases.

Dissipation factor of qSV waves at 50 Hz for cases 1, 2 and 3



qSV anisotropy is strong for angles between 30 and 60 degrees. The lossless case 2 is represented by a triangle at the origin.

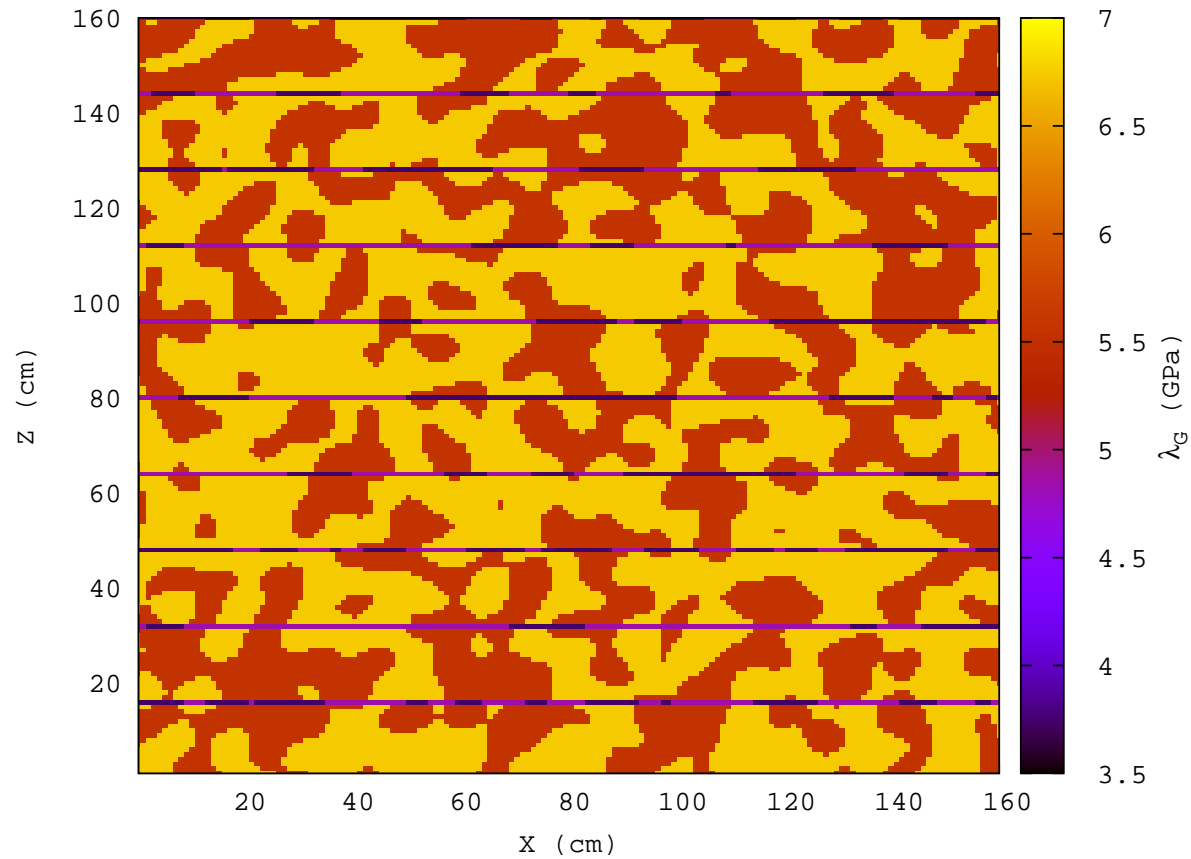
Polar representation of the qSH energy velocity vector at 50 Hz for cases 1, 2 and 3



SH velocity anisotropy is observed to be induced by fractures. Cases 1 and 3 are almost indistinguishable.

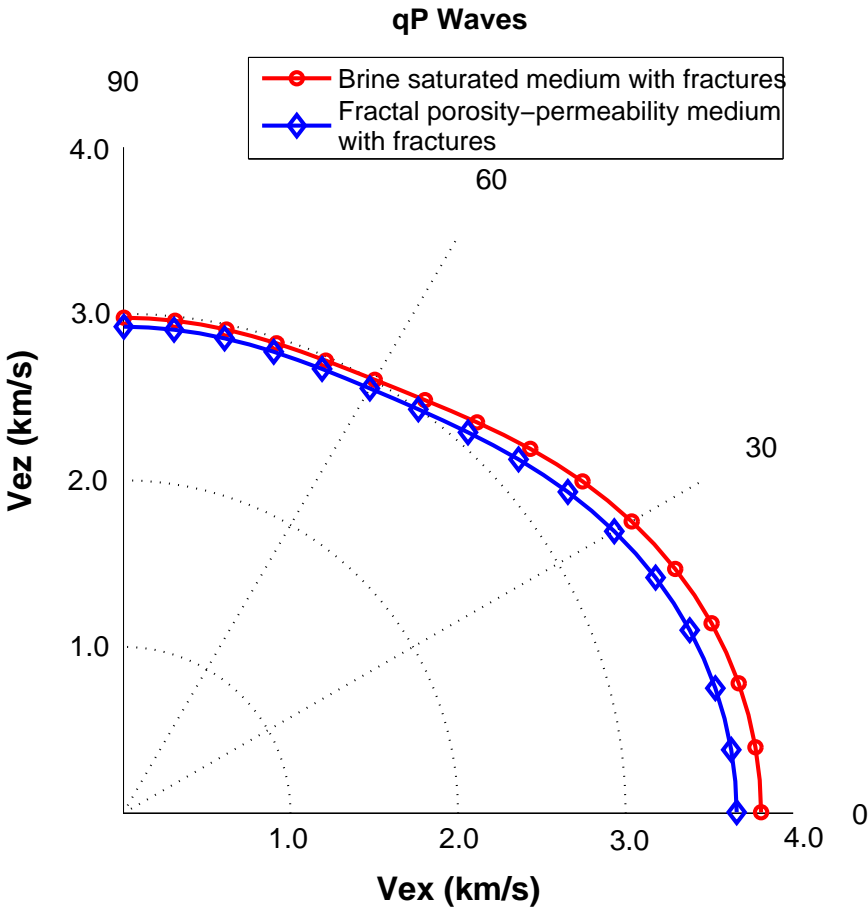
Velocity for case 2 is isotropic. SH waves are lossless, since p_{55} and p_{66} are real.

Lamé coefficient (GPa) for the brine-saturated fractal porosity-permeability sample of case 4.



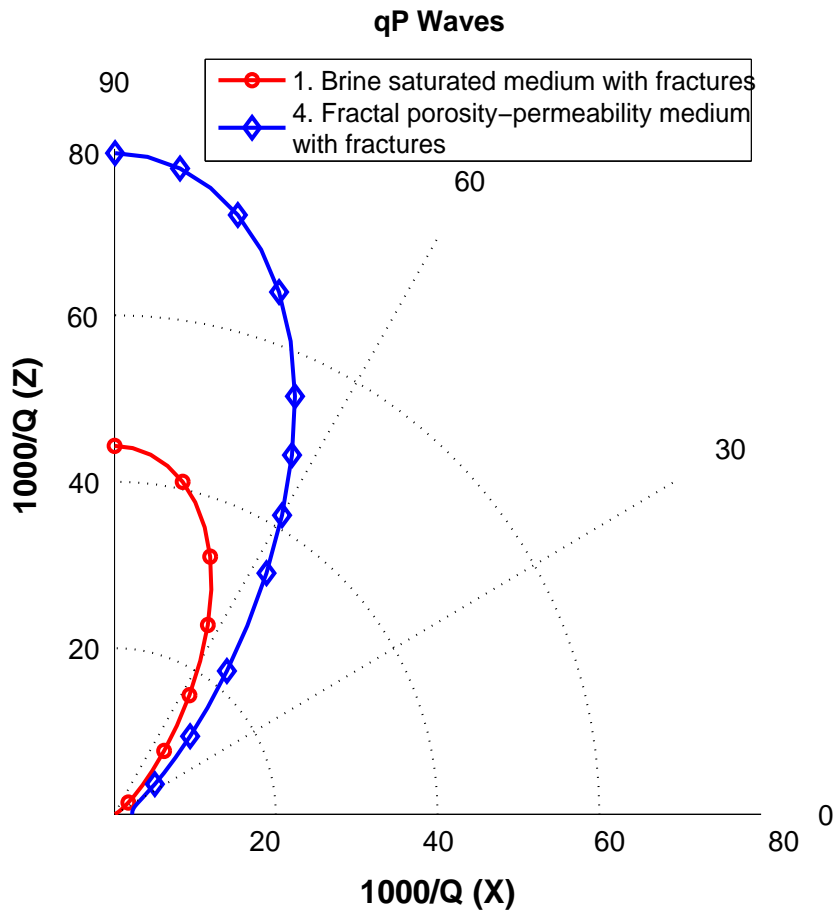
$\log \kappa(x, z) = \langle \log \kappa \rangle + f(x, z)$, $f(x, z)$: fractal representing the spatial fluctuation of the permeability field $\kappa(x, z)$.

Polar representation of the qP energy velocity vector at 50 Hz for cases 1 and 4.



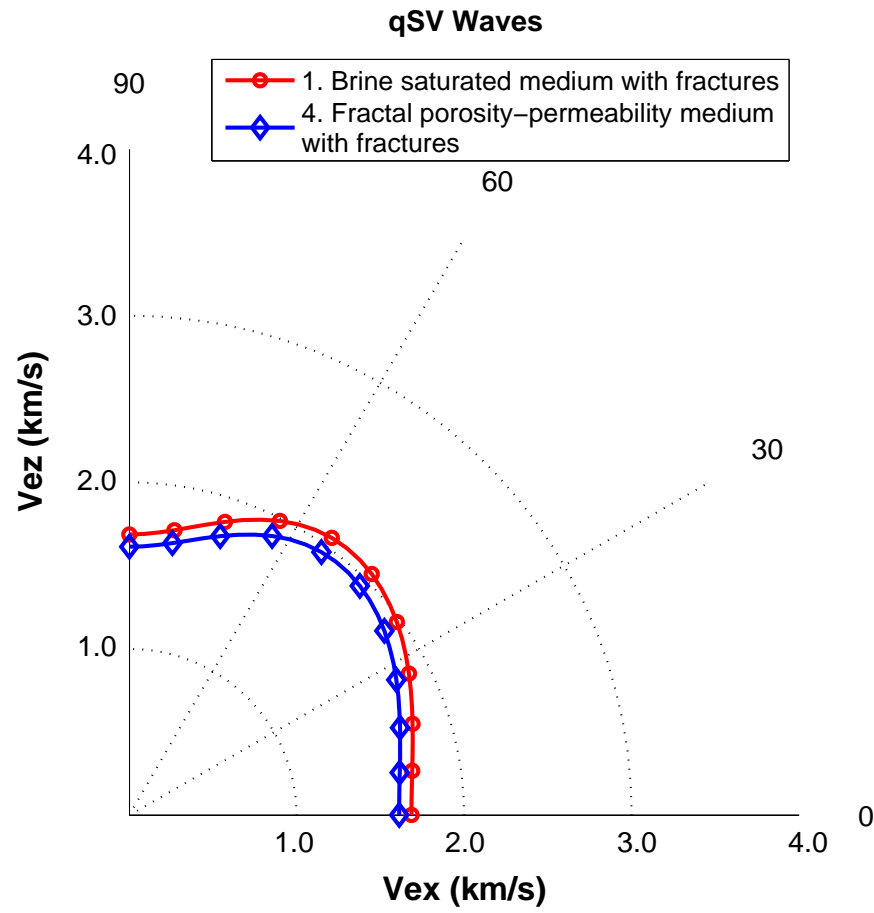
Note the increase in Q anisotropy for qP waves for angles normal to the fracture plane.

Dissipation factor of qP waves at 50 Hz for cases 1 and 4.



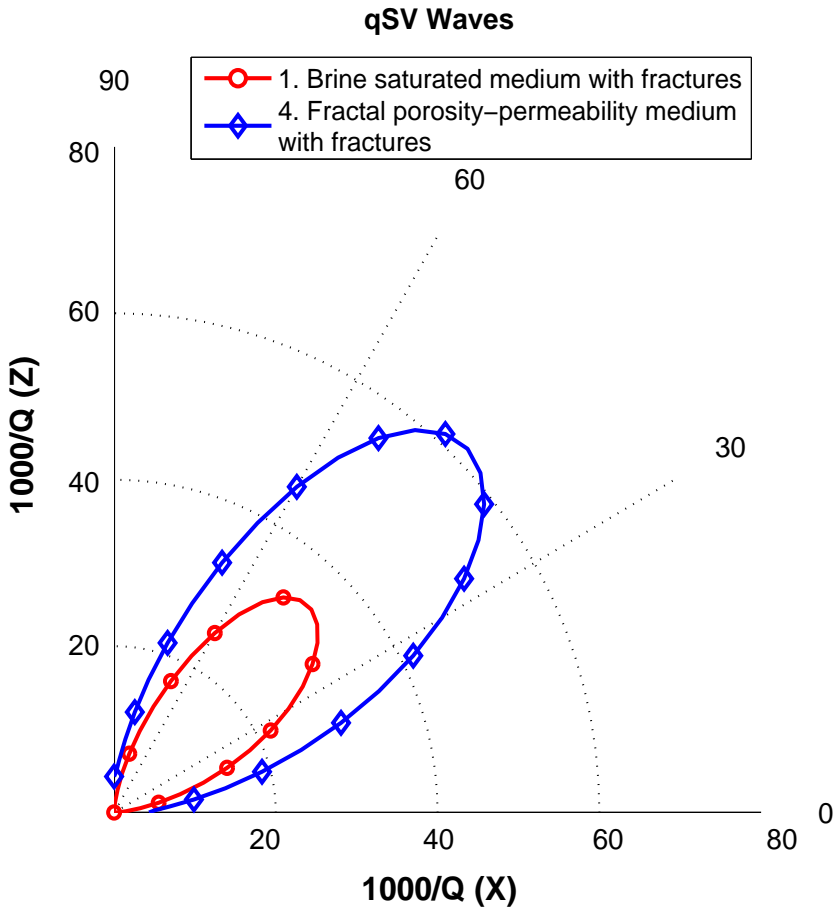
Note the increase in Q anisotropy for qP waves for angles normal to the fracture plane.

Polar representation of the qSV energy velocity vector at 50 Hz for cases 1 and 4.



Note the energy velocity reduction in the heterogeneous case.

Dissipation factor of qSV waves at 50 Hz for cases 1 and 4.



Note the increase in Q anisotropy for angles between 30 and 60 degrees. Also, velocity anisotropy is less affected by frame heterogeneities than Q-anisotropy.

The Macroscale I. Seismic modeling. Variational formulation

We solve the following boundary value problem at the macroscale in a domain Ω with boundary $\partial\Omega$:

$$-\omega^2 \rho u - \nabla \cdot \tau(u) = F, \quad \Omega$$

$$-\tau(u)\nu = i\omega \mathcal{D}u, \quad \partial\Omega, \text{ (absorbing boundary condition, } D > 0)$$

$u = (u_x, u_z)$: displacement vector, ρ : average density.

$\tau(u)$: stress-tensor of our **equivalent TIV medium**, defined in terms of the p'_{IJ} s.

A global continuous variational formulation: Find $u(x, \omega) \in [H^1(\Omega)]^2$ **such that**

$$-(\rho\omega^2 u, \varphi) + (\tau(u), \varepsilon(\varphi)) + i\omega \langle \mathcal{D}u, \varphi \rangle_{\partial\Omega} = (f, \varphi), \quad \varphi \in [H^1(\Omega)]^2,$$

The Macroscale. II. Global continuous and FE variational formulation.

\mathcal{T}^h : a partition of $\bar{\Omega}$ into rectangles of diameter bounded by h :

$$\bar{\Omega} = \cup_{j=1}^J \Omega_j$$

$\Gamma_j = \partial\Omega \cap \partial\Omega_j$, $\Gamma_{jk} = \Gamma_{kj} = \partial\Omega_j \cap \partial\Omega_k$; ξ_{jk} the centroids of Γ_j and Γ_{jk} .

Reference rectangular element

$$R = [-1, 1]^2, \quad S(R) = \text{Span} \left\{ 1, x, z, \left(x^2 - \frac{5}{3}x^4 \right) - \left(z^2 - \frac{5}{3}z^4 \right) \right\}.$$

The DOF associated with S : values at the mid points of the faces of R .

If $a_1 = (-1, 0)$, $a_2 = (0, -1)$, $a_3 = (1, 0)$ and $a_4 = (0, 1)$,

the basis function

$$\psi_1(x, z) = \frac{1}{4} - \frac{1}{2}x - \frac{3}{8} \left[\left(x^2 - \frac{5}{3}x^4 \right) - \left(z^2 - \frac{5}{3}z^4 \right) \right]$$

is such that

$$\psi_1(a_1) = 1 \text{ and } \psi_1(a_j) = 0, j = 2, 3, 4.$$

The Macroscale. III. Global FE variational formulation.

The nonconforming FE space \mathcal{NC}^h

$$\mathcal{NC}^h = \{\varphi \in [L^2(\Omega)]^2 : \varphi_j \in [S(\Omega_j)]^2, \quad \varphi_j(\xi_{jk}) = \varphi_k(\xi_{jk}) \forall j, k\},$$

φ_j : the restriction of φ as seen from Ω_j . The global nonconforming FE

procedure: Find $u^h \in \mathcal{NC}^h$ such that

$$-(\rho\omega^2 u^h, \varphi) + \sum_j (\tau(u^h), \varepsilon(\varphi))_{\Omega_j} + i\omega \langle \mathcal{D}u^h, \varphi \rangle_{\partial\Omega} = (f, \varphi), \quad \varphi \in \mathcal{NC}^h.$$

Instead of solving the global algebraic problem associated with the global FE procedure above, we will employ the iterative domain decomposition procedure.

The Macroscale. IV. FE Domain decomposition.

Consider the decomposed problem over Ω_j satisfying the interface consistency conditions

$$\tau_{jk}\nu_{jk} + i\beta_{jk}u_j = -\tau_{kj}\nu_{kj} + i\beta_{jk}u_k, \quad x \in \Gamma_{jk} \subset \partial\Omega_j,$$

$$\tau_{kj}\nu_{kj} + i\beta_{jk}u_k = -\tau_{jk}\nu_{jk} + i\beta_{jk}u_j, \quad x \in \Gamma_{kj} \subset \partial\Omega_k,$$

β_{jk} : positive definite iteration matrix functions defined on the interior boundaries Γ_{jk} .

To localize the calculations, we introduce a set of Lagrange multipliers

λ_{jk}^h : associated with the stress values $-\tau(u_j)\nu_{jk}(\xi_{jk})$:

$$\tilde{\Lambda}^h = \{\lambda^h : \lambda^h|_{\Gamma_{jk}} = \lambda_{jk}^h \in [P_0(\Gamma_{jk})]^2 = [\Lambda_{jk}^h]^2\}.$$

$P_0(\Gamma_{jk})$ are constant functions on Γ_{jk} . Note that Λ_{jk}^h and Λ_{kj}^h are considered to be distinct.

The Macroscale. V. FE Domain Decomposition Iteration.

Given an initial guess $\left(\widehat{u}_j^{h,0}, \lambda_{jk}^{h,0}, \lambda_{kj}^{h,0}\right) \in [NC_j^h]^2 \times [\Lambda_{jk}^h]^2 \times [\Lambda_{kj}^h]^2$,
compute $\left(\widehat{u}_j^{h,n}, \lambda_{jk}^{h,n}\right) \in [NC_j^h]^2 \times [\Lambda_{jk}^h]^2$ **as the solution of the equations**

$$\begin{aligned}
 & -(\rho\omega^2 \widehat{u}_j^{h,n}, \varphi)_j + \sum_{pq} (\tau_{pq}(\widehat{u}^{h,n}), \varepsilon_{pq}(\varphi))_j + i\omega \left\langle \left\langle \mathcal{D}\widehat{u}_j^{h,n}, \varphi \right\rangle \right\rangle_{\Gamma_j} \\
 & + \sum_k \left\langle \left\langle \lambda_{jk}^{h,n}, \varphi \right\rangle \right\rangle_{\Gamma_{jk}} = (\widehat{f}, \varphi)_j, \quad \varphi \in [NC_j^h]^N, \\
 & \lambda_{jk}^{h,n} = -\lambda_{kj}^{h,n-1} + i\beta_{jk} [\widehat{u}_j^{h,n}(\xi_{jk}) - \widehat{u}_k^{h,n-1}(\xi_{jk})], \quad \text{on } \Gamma_{jk}.
 \end{aligned}$$

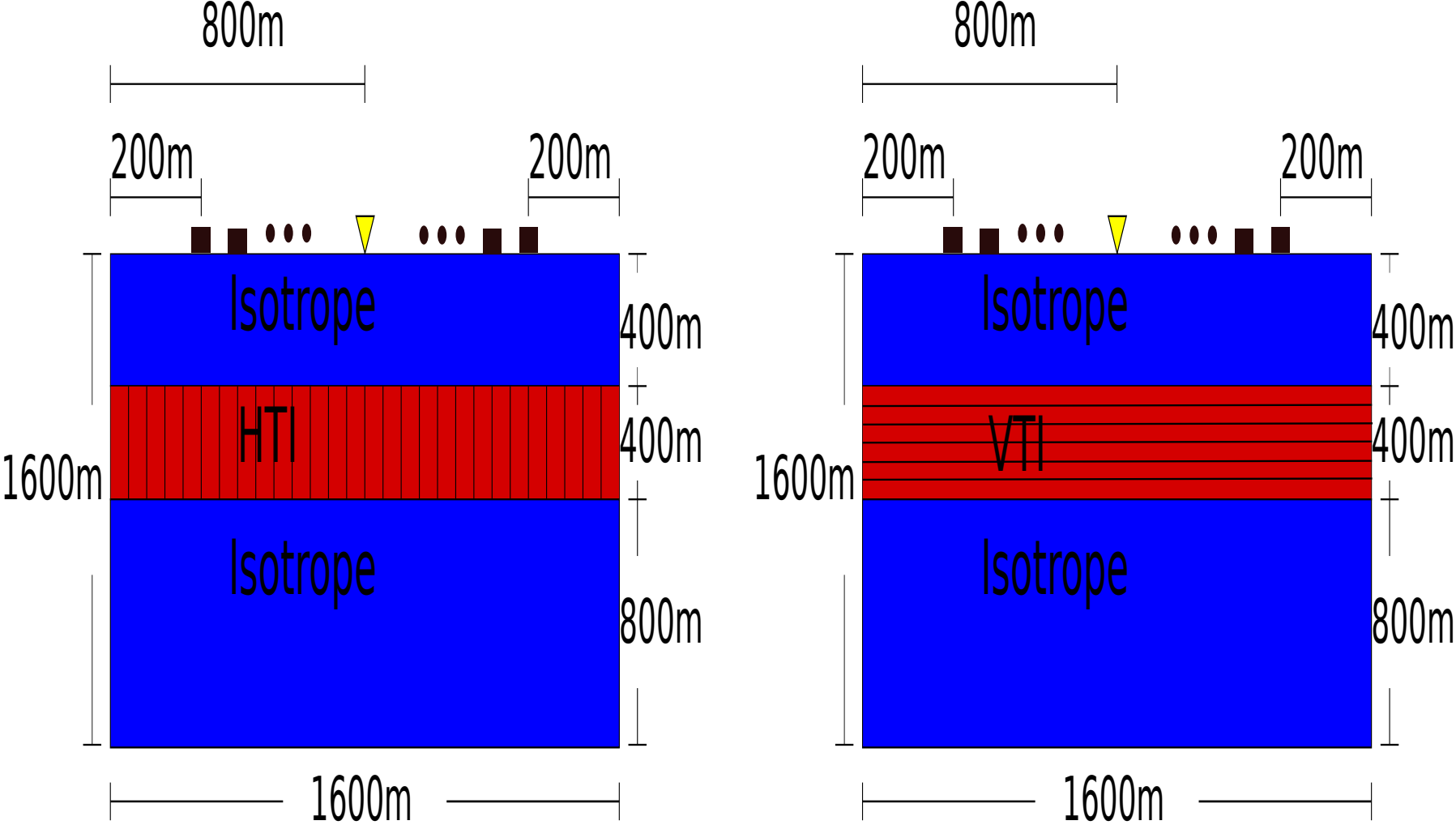
It can be shown that if u^h is the solution of the global FE procedure,

$$\|\widehat{u}^{h,n} - u^h\|_0 \rightarrow 0 \text{ in } [L^2(\Omega)]^2 \quad \text{when } n \rightarrow \infty,$$

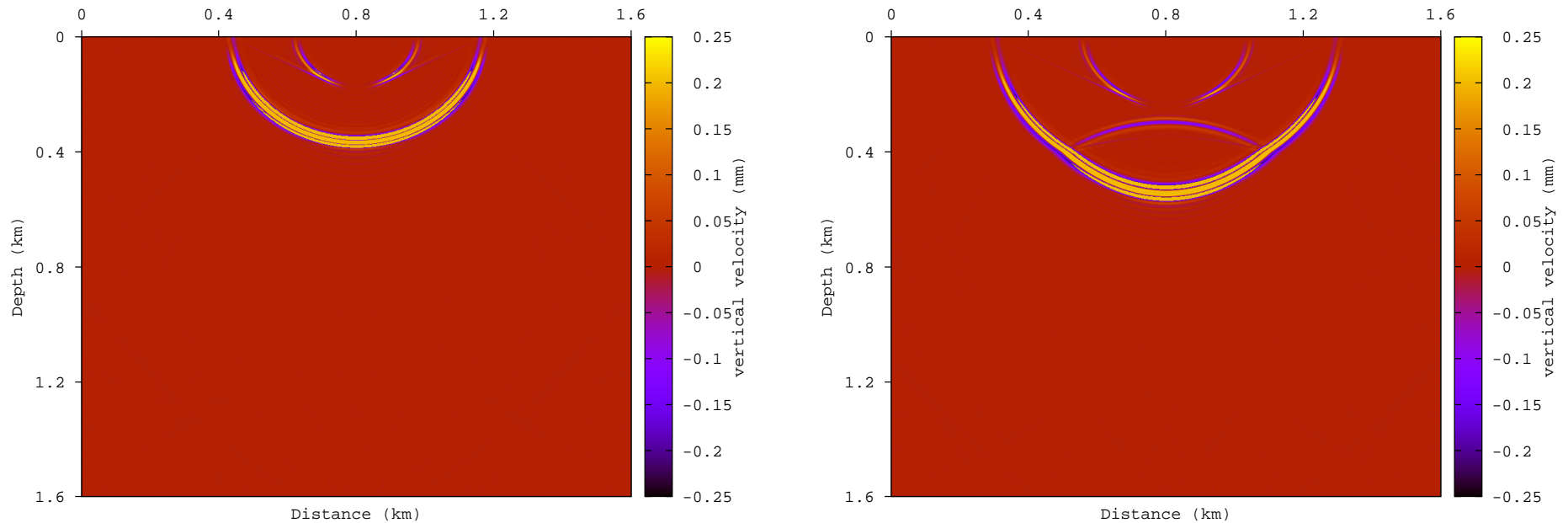
- The macroscopic model consists of an isotropic square background Ω of 1.6 km side length containing an anisotropic layer of 400m thickness of either horizontal or vertical aligned fractures (HTI or VTI medium).
- The stiffnesses coefficients of the anisotropic layer are those determined using the harmonic experiments, for the cases of fully brine saturated fractures (Case 1) or 10 % patchy CO₂ saturation (Case 3).
- The isotropic background has P- and S-wave velocities at 50 Hz equal to 2633 m/s and 1270 m/s, respectively.

- For the HTI-case, qP- and qSV-wave velocities at 50 Hz are equal to 3808. m/s and 1686 m/s, respectively, while for the VTI-case qP- and qSV-wave velocities at 50 Hz are equal to 3008. m/s and 1686 m/s, respectively
- The computational mesh consists of square cells having side length 4 m, and The source is a dilatational perturbation of central frequency is 50 Hz, located at $(x = 800m, z = 6.m)$.

The Macroscale Model. III

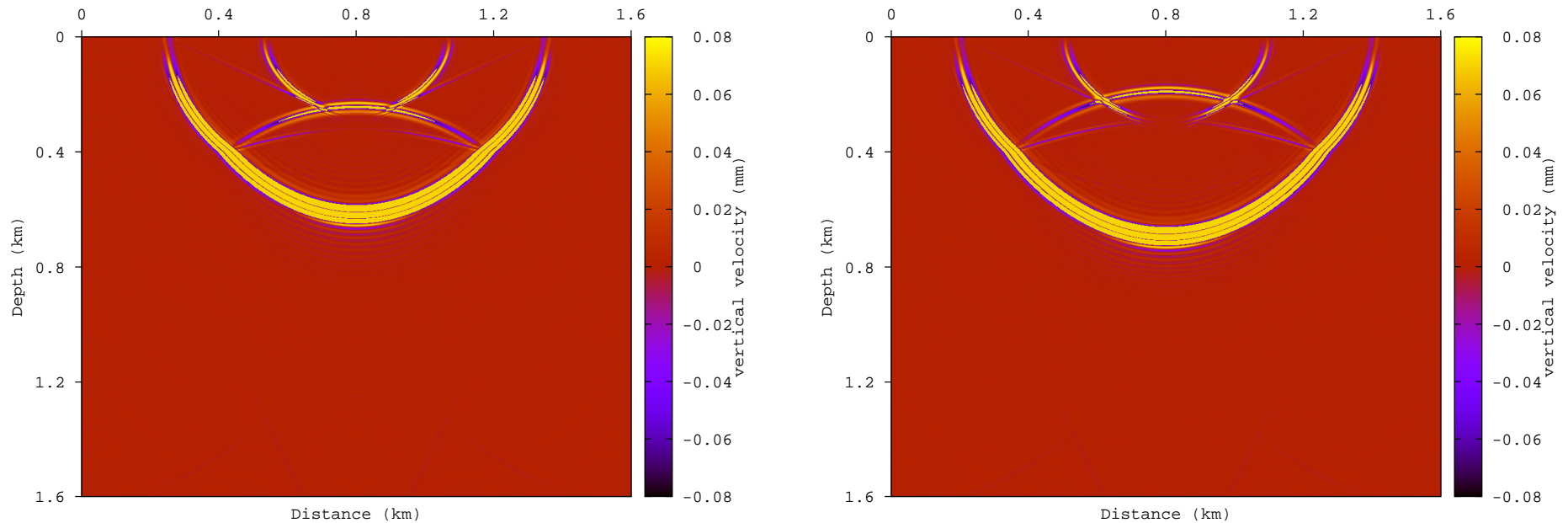


Snapshots of z-component of velocity at 150ms (left) and 200 ms (right). HTI brine saturated fractures.



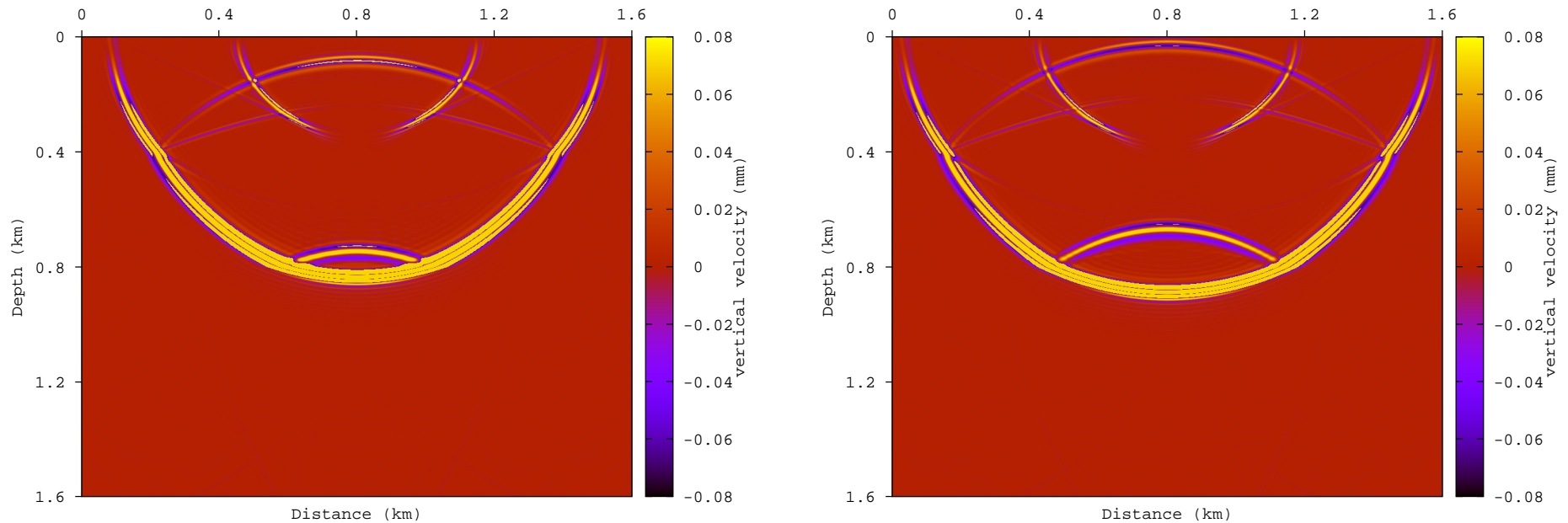
At 150 ms the incident P-wave is arriving to the top of the HTI layer. At 200 ms a reflected P-wave travelling upwards and a transmitted qP-wave travelling downwards are observed. The other wavefronts are S-waves generated by the point source at the top boundary.

Snapshots of z-component of velocity at 220ms (left) and 240 ms (right). HTI brine saturated fractures.



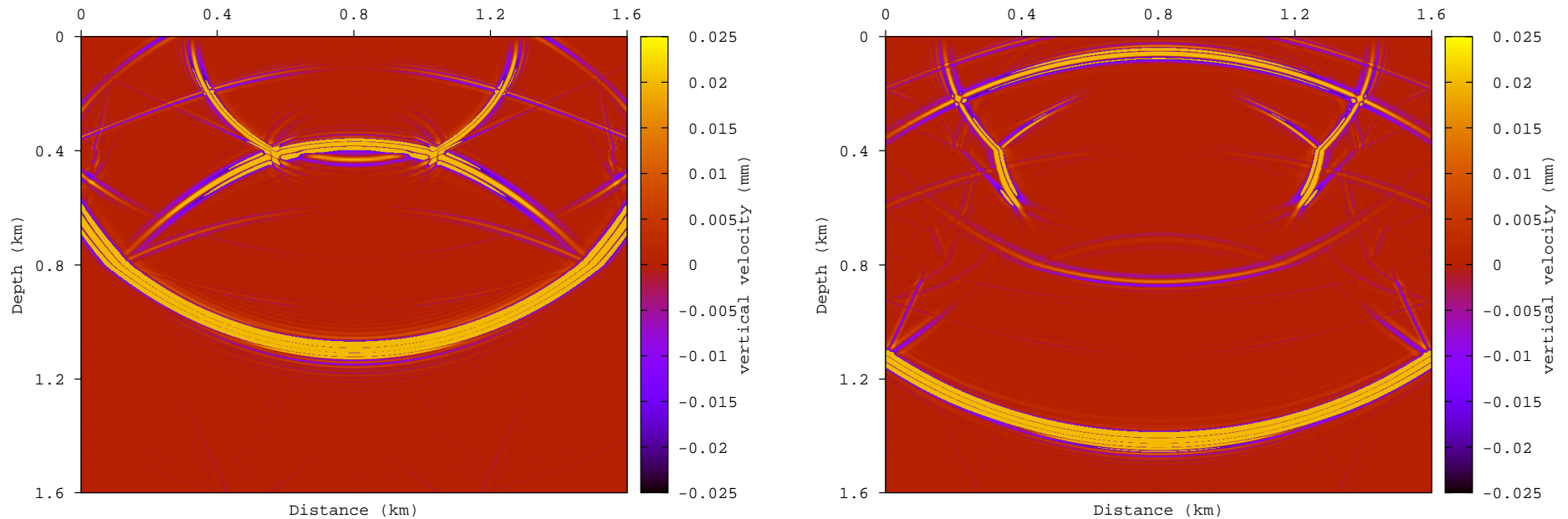
At 220 ms and 240 ms a reflected P-wave and travelling upwards and a transmitted qP-wave travelling downwards are observed. Note the deformation of the qP-wavefront because of the anisotropy in the HTI layer. The other (thin) wavefronts are S-waves generated by the point source at the top boundary.

Snapshots of z-component of velocity at 280ms (left) and 300 ms (right). HTI brine saturated fractures.



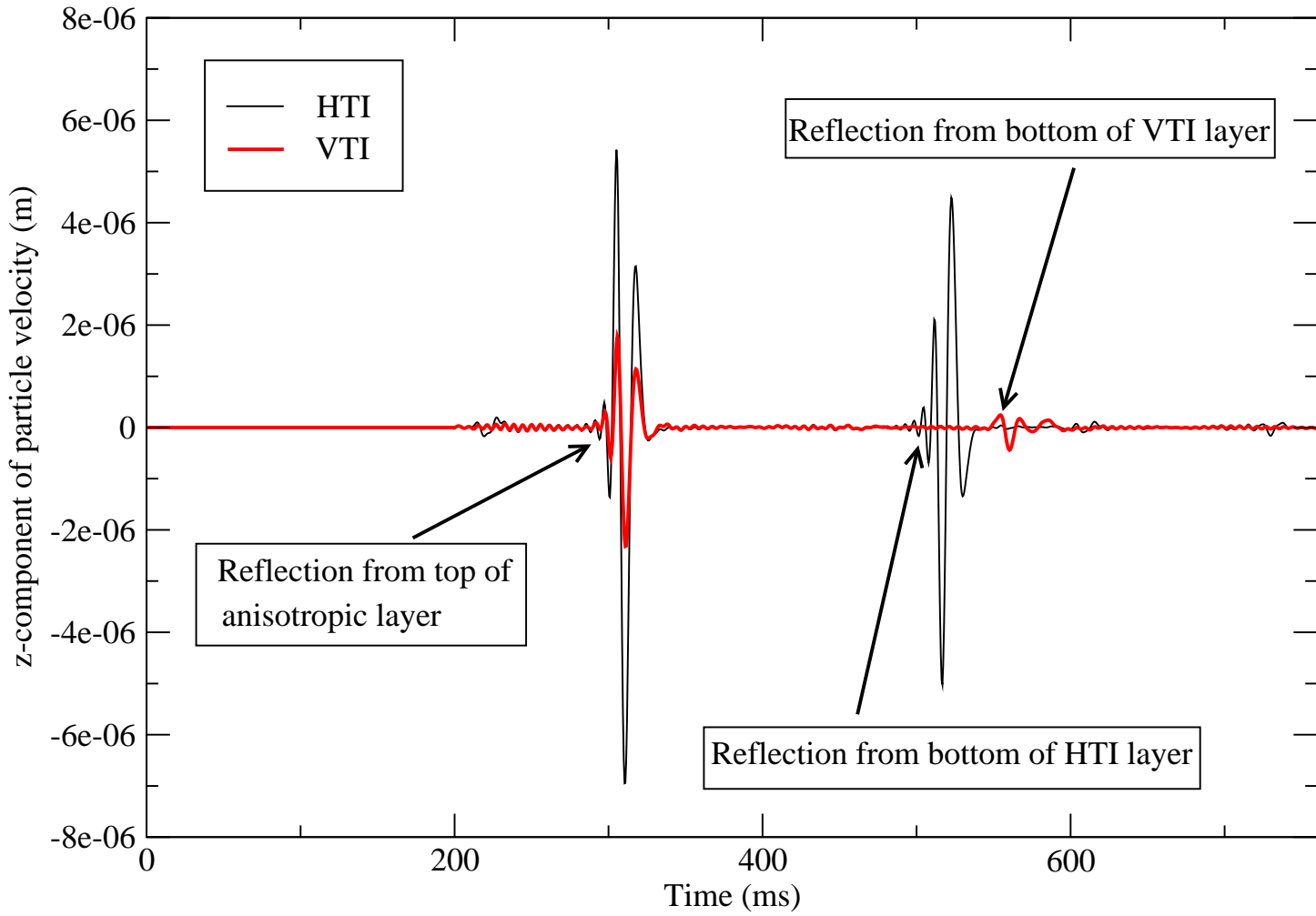
At 280 and 300 ms we can observe an upcoming P-wavefront and a tiny upcoming S-wavefront reflected at the top of the HTI layer and an upcoming qP-wavefront generated by reflection of the downgoing qP-wave at the bottom of the HTI layer. At 300 ms the reflected P-wave generated at the top of the HTI layer is arriving at the surface geophones.

Snapshots of z-component of velocity at 380ms (left) and 500 ms (right). HTI brine saturated fractures.

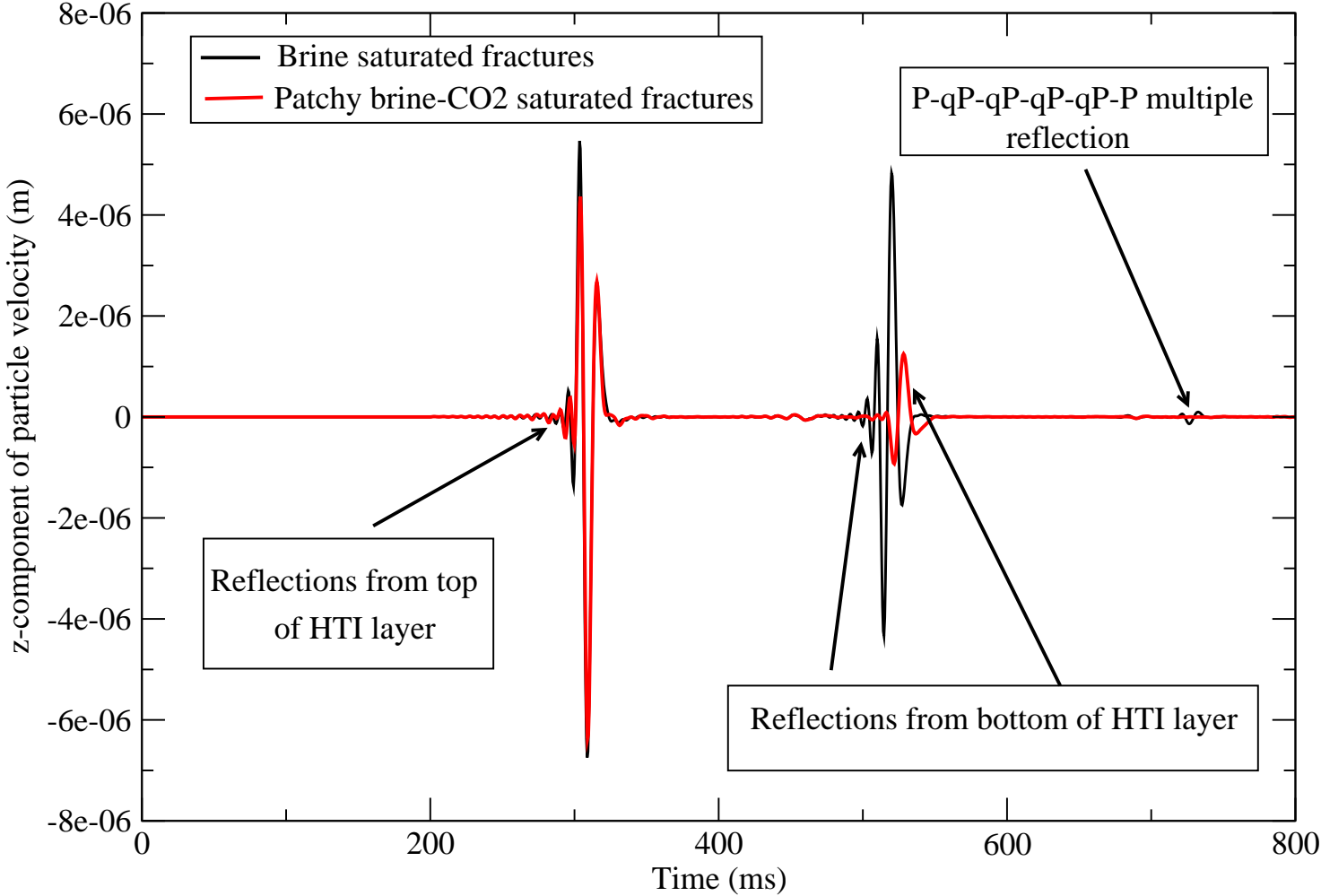


At 380 and 500 ms we can observe the reflected S-wave arriving at the surface geophones, together with the qP-P wave reflected at the bottom of the HTI layer. The transmitted qP wave has already left the HTI layer and continues travelling downwards as a converted P-wave. Conversions to S-waves can also be seen in both snapshots

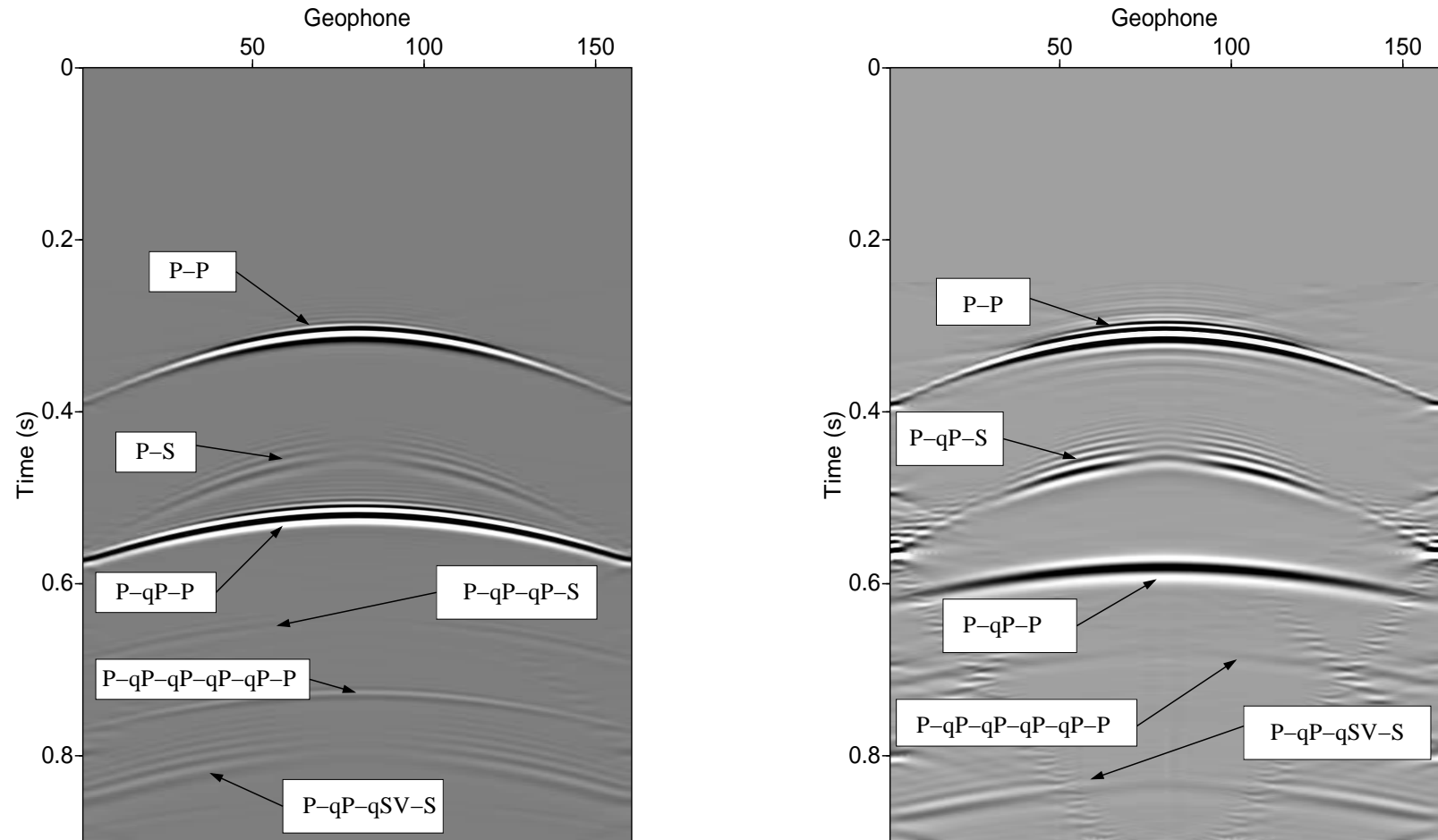
Synthetic traces. HTI and VTI brine saturated fractures.



Synthetic traces. HTI brine and patchy brine-CO₂ saturated fractures.

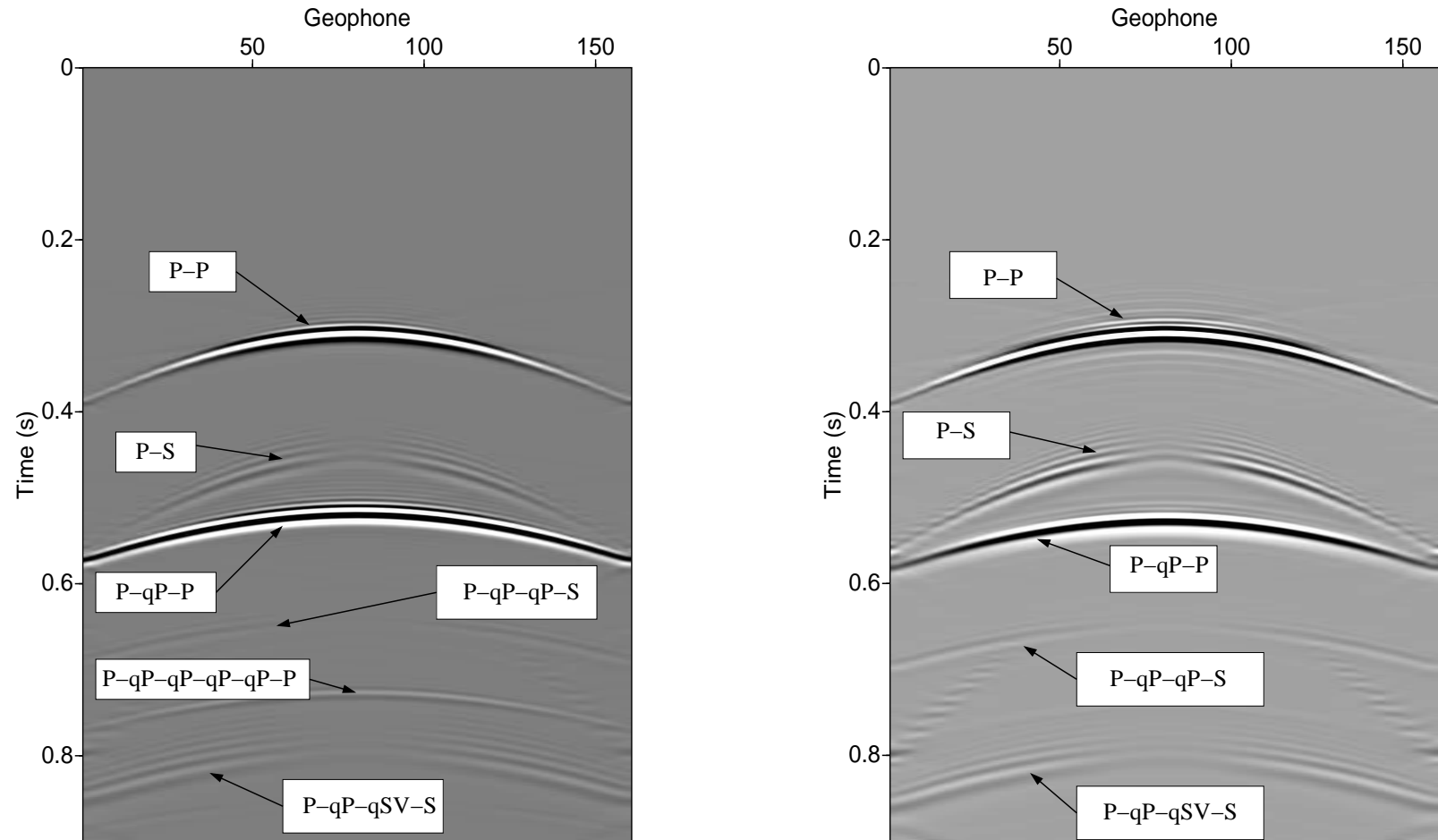


Synthetic seismograms. HTI (left) and VTI (right) brine saturated fractures.



The seismograms show the arrivals of P and S waves reflected at the top of the HTI and VTI layers, as well as later arrivals corresponding to conversions from incident P to qP and qSV waves at the top and bottom of the layers. In particular, it is clearly seen the late **P-qP-P arrival** of the VTI case as compared with the corresponding one in the HTI case. The qP-velocities in the HTI and VTI layers are about 3800 m/s and 3000m/s, respectively.

Synthetic seismograms. HTI brine (left) and 10 % CO₂ (right) saturated fractures.



The seismograms show the arrivals of P and S waves reflected at the top of the HTI layer, and later arrivals corresponding to conversions from incident P to qP and qSV waves at the top and bottom of the layer. In particular, the **P-qP-qP-qP-qP-qP-P arrival** in the brine-saturated case is not seen in the patchy brine-CO₂ case due to the strong attenuation of qP waves when CO₂ is present ($Q_p \approx 10$ at normal incidence). Instead qSV-waves are less attenuated when CO₂ is present and the **P-qP-qSV-S-arrival** is still observed.

Conclusions

- Numerical upscaling procedures allow to represent poroelastic samples with a dense set of aligned fractures at the mesoscopic-scale saturated by different fluids, bringing the induced anisotropy at the macroscale.
- THE FEM is a useful tool to solve local problems at the mesoscale in the context of Numerical Rock Physics and global wave propagation problems at the macroscale.
- The techniques presented here to model acoustics of porous media in geophysics can be extended to other fields, like ultrasound testing of quality of foods, groundwater flow and contamination among others.
- Thanks for your attention !!!!!.